Development of a Multiuse Human-Scale Single-Ring OpenPET System

Hideaki Tashima, *Member, IEEE*, Eiji Yoshida, Yuma Iwao, Hidekatsu Wakizaka, Akram Mohammadi, *Member, IEEE*, Munetaka Nitta, Atsushi Kitagawa, Taku Inaniwa, Fumihiko Nishikido, Atsushi B. Tsuji, Yuji Nagai, Chie Seki, Takafumi Minamimoto, Yasuhisa Fujibayashi, and Taiga Yamaya, *Member, IEEE*

***Abstract*—We developed a human-scale single-ring OpenPET (SROP) system, which had an open space allowing us access to the subject during measurement. The SROP system consisted of 160 4-layer depth-of-interaction detectors. The open space with the axial width of 430 mm was achieved with the ring axial width of 214 mm and the ring inner diameter of 660 mm. The detectors were axially shifted to each other so that the detector ring was aligned along a plane horizontally tilted by 45° against the axial direction. The system was developed as a mobile scanner to be used not only in clinical positron emission tomography (PET) rooms but also in charged-particle therapy treatment rooms as well as animal experiment rooms. Almost uniform spatial resolution better than 3 mm throughout the entire field of view (FOV) was realized with an iterative image reconstruction method. Peak absolute sensitivity was 3.1%, and there was a region with sensitivity better than 0.8% for a length of more than 700 mm. An in-beam imaging experiment conducted at the heavy ion medical accelerator in Chiba showed that the system was operable even at the highest beam intensity available for heavy-ion therapy. In addition, we conducted entire-body monkey dynamic imaging utilizing the long region inside the gantry by positioning a monkey along the direction having the longest FOV tilted by 45° against the axial direction. We concluded the developed system has a capability to realize versatile PET applications by utilizing its wide-open space and mobility in addition to high spatial resolution with sufficiently good sensitivity.**

***Index Terms*—Depth-of-interaction (DOI) detector, in-beam positron emission tomography (PET), OpenPET, PET, single-ring OpenPET (SROP).**

Manuscript received April 24, 2020; revised August 20, 2020 and October 19, 2020; accepted November 2, 2020. Date of publication November 10, 2020; date of current version November 3, 2021. This work was supported in part by the Japan Society for the Promotion of Science (JSPS) KAKENHI under Grant 25242052 and Grant 19KK0280, and in part by the QST President's Strategic Grant (Creative Research). *(Corresponding author: Hideaki Tashima.)*

The authors are with the National Institute of Radiological Sciences, QST, Chiba 263-8555, Japan (e-mail: tashima.hideaki@qst.go.jp; yoshida.eiji@qst.go.jp; iwao.yuma@qst.go.jp; wakizaka.hidekatsu@qst.go.jp; mohammadi.akram@qst.go.jp; nitta.munetaka@qst.go.jp; kitagawa.atsushi@qst.go.jp; inaniwa.taku@qst.go.jp; nishikido.fumihiko@qst.go.jp; tsuji.atsushi@qst.go.jp; nagai.yuji@qst.go.jp; seki.chie@qst.go.jp; minamimoto.takafumi@qst.go.jp; fujibayashi.yasuhisa@qst.go.jp; yamaya.taiga@qst.go.jp).

Color versions of one or more figures in this article are available at https://doi.org/10.1109/TRPMS.2020.3037055.

Digital Object Identifier 10.1109/TRPMS.2020.3037055

I. Introduction

WE HAVE developed a series of open-type positron emission tomography (PET) systems, OpenPET, which can provide a physically opened space accessible during measurement [1]–[8]. One of the applications of OpenPET is in-beam PET for range verification of particle therapy, such as proton therapy and carbon ion therapy, in which positron emitters are generated via fragmentation reactions, and the Bragg peak position can be estimated from PET images [9]–[11]. The range verification for particle therapy is an active research area. In addition to PET-based methods using dual-head or partial ring geometries to allow the beam to pass through [12]–[24], collimators-based [25]–[28], timing-based [29], [30], and Compton camera techniques-based [31]–[35] methods targeting prompt gamma rays are being studied. Although these methods are classified as 2-D or limited angle imaging, OpenPET has the potential to acquire highly accurate 3-D images because of its full ring geometry.

Fig. 1 summarizes OpenPET research studies in the progression toward in-beam application. The OpenPET geometries can be mainly categorized into two groups, dual-ring OpenPET (DROP) and single-ring OpenPET (SROP). OpenPET is made possible by depth-of-interaction (DOI) detectors [36]–[39] that suppress the parallax error because most of the lines of response (LORs) in the OpenPET geometries are oblique. The idea for OpenPET first came up as the DROP geometry [1]. After showing a proof-of-concept with a small prototype [2], we developed a human-sized system [7]. The DROP geometry consists of two cylindrical detector rings axially separated with an open space. On the other hand, the SROP geometry was proposed as a more efficient geometry for in-beam applications because of its wide open space and high sensitivity. The SROP geometry has a cylinder shape cut by two parallel planes tilted against the axial direction to form an open space. The tilt angle can be calculated from the desired open space width, the detector ring axial width, and the bed width (cylinder diameter). We also showed that the SROP geometry has higher sensitivity and a smaller size than the slant arrangement of a cylindrical PET [12] which can provide a treatment beam path for in-beam PET measurement. The SROP geometry allows the beam port to be at the closest possible point to the patient [3]. These advantages outweigh the manufacturing cost of using the DOI detectors

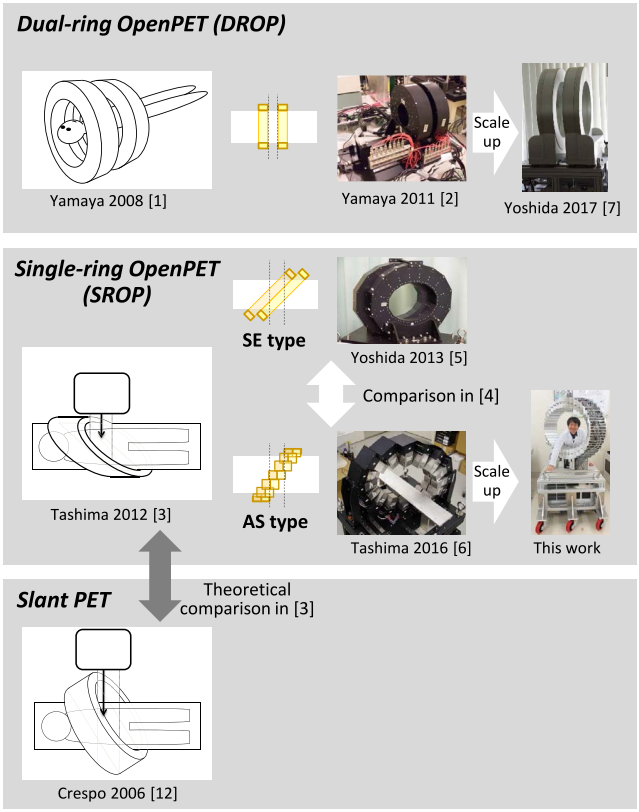

Fig. 1. Summary of OpenPET research studies.

to realize the SROP system. To implement the SROP with block detectors, we investigated two arrangement methods: 1) a slant-ellipsoid (SE) type in which ellipsoidal rings are arranged along the bedside and 2) an axial-shift (AS) type in which detectors are axially shifted along the plane tilted against the axial direction. We previously compared these two types arranged with DOI detectors by simulation and found no significant difference in image quality [4]. Based on the two types of SROP detector arrangement methods, we have developed two small prototype systems [5], [6]. Although the imaging performance was not significantly different, we found that the AS-type SROP geometry was compacter and easier to manufacture than the SE-type SROP geometry requiring the design of ellipsoidal block rings.

In this study, we developed a human-scale OpenPET system having the largest open space achieved yet based on the AS-type SROP geometry. The human-scale SROP system provides a wider open space than the previous DROP system without increasing the number of detectors relative to the DROP configuration. The wide-open space enables multiple PET applications in addition to in-beam PET. One of the potential applications is online or real-time PET image guided surgery, which can prevent tumors from being missed or left after surgery while minimizing the resection area to maximize a patient's quality of life [40]. We should note that the wide-open space increases the oblique angle of the LORs and the parallax error. Therefore, we need to evaluate carefully the effectiveness of the DOI detectors for the human-scale SROP system to maintain uniformity of the spatial resolution.

We developed our system as a mobile and multiuse PET scanner to be employed not only in clinical PET rooms but also in various types of treatment rooms such as irradiation rooms in the heavy ion medical accelerator in Chiba (HIMAC) as well as animal experiment rooms for preclinical studies. After a basic performance evaluation, we carried out an in-beam experiment in one irradiation room of the HIMAC. Also, in an animal experiment room, we demonstrated a dynamic entire-body monkey scan utilizing a wide field of view (FOV) in the direction detectors were aligned.

II. Materials and Methods

A. SROP Geometry

The SROP system was designed based on the components of the DROP system [7] and a whole-body DOI PET system [41]. Fig. 2 shows a conceptual illustration and design sketches. The SROP system was designed with 4 axially shifted detector rings of 40 DOI detectors each. The ring diameter was 660 mm and the total axial length was 214 mm. The ring was aligned on a plane slanted by 45° from the axial direction (z direction) to obtain an open space of 430 mm. The shift of each detector compared with a conventional cylindrical geometry with the same total axial length can be calculated as follows. We let the angles of x and y directions on the x-y plane be 0° and 90°, respectively, the z position of a detector whose center is located on the angle of θ is shifted by

$$-\frac{W+C}{2}\cos\theta \tag{1}$$

where W is the total axial length of the detector ring and C is the width of the open space.

B. Sensitivity Prediction

The sensitivity varies depending on the width of the open space. The human-scale DROP system was developed with a changeable open space size achievable by a shifting mechanism of the rings. However, achieving the human-scale SROP system with a changeable open space size was difficult as the detectors required for the human-scale were too heavy. Therefore, we first conducted a Monte Carlo simulation using the Geant4 tool kit [42] to predict the sensitivity at the FOV center of the SROP compared with that of the DROP to show the effectiveness of the SROP geometry for achieving high sensitivity with various open space sizes. The sensitivity was calculated as the ratio of detected coincidence count against the number of generated annihilation photon pairs. We varied the open space width from 90 mm to 430 mm. In both geometries, 160 detectors were arranged in 4 rings with the ring diameter of 660 mm. In the case of SROP, the amount of axial shift for each detector was calculated by (1) with $C = 90$ mm to 430 mm. The open space for the DROP was adjusted as the axial distance between two detector rings. Sensitivity values were normalized with a normalization factor calculated by dividing the actually measured sensitivity of the DROP system with the open space of 90 mm [7] by the sensitivity obtained by simulation. This step was necessary because the actual system contained many factors that the simulation did not incorporate. Because we used the same detector and components as the DROP system, we expected that the normalized values for the SROP would be highly accurate.

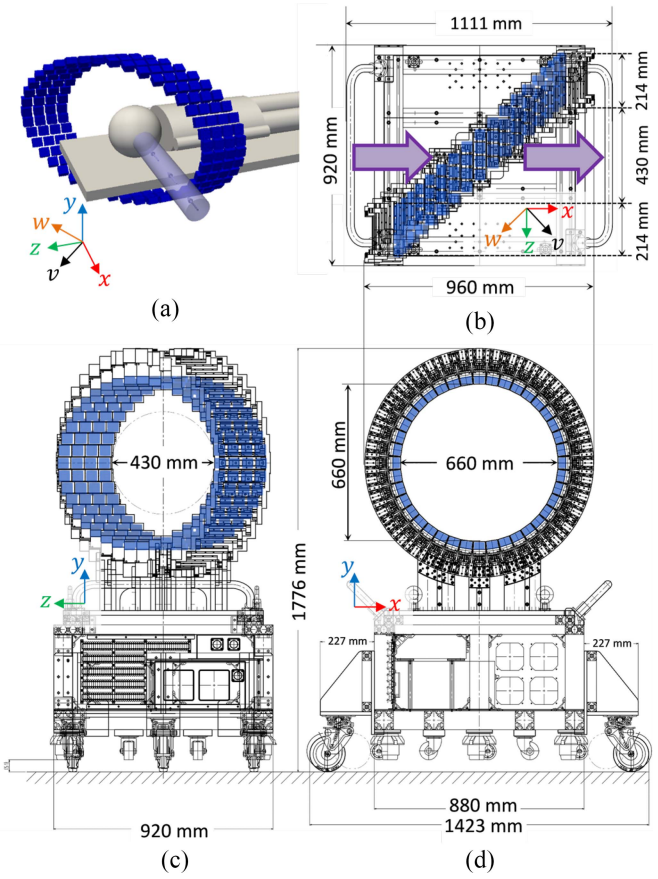

Fig. 2. Conceptual illustration of SROP (a) and design sketches: top (b), side (c), and front (d) views. The blue blocks indicate scintillator blocks. The red, blue, green, black, and orange arrows indicate the *x*, *y*, *z*, *v*, and *w* directions defined in the system, for which the origin is the FOV center.

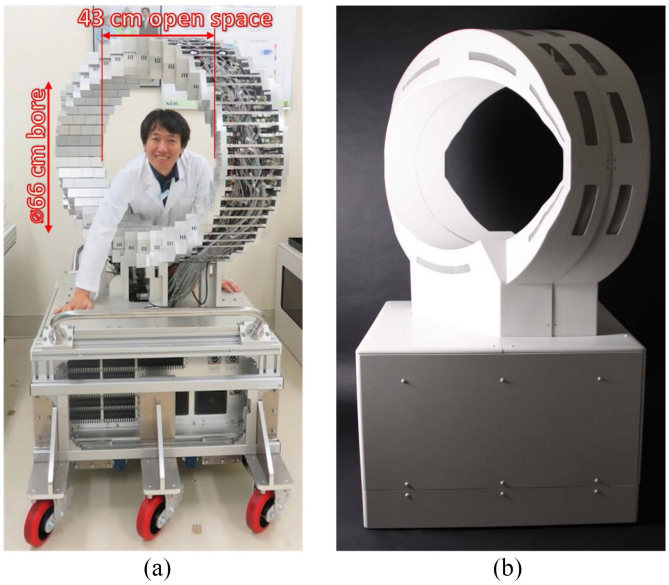

Fig. 3. Developed SROP system (a) and gantry cover (b).

C. Development of the SROP System

Fig. 3 is a photograph of the developed SROP system and Table I lists specifications of the system. The gantry had 6 wheels for good mobility. We used 160 DOI detectors in total. Each of the DOI detectors was composed of an array of $16 \times 16 \times 4$ Zr-doped gadolinium oxorthosilicate (GOSZ) scintillator crystals with dimensions of $2.8 \times 2.8 \times 7.5$ mm^3 and a 64-ch photomultiplier tube (PMT) with a super-bialkali photocathode (Hamamatsu R10552-100-M64) [39]. The detectors with front-end circuits were connected to a data acquisition (DAQ) system with 7-m coaxial cables to protect the electronics circuits from radiation damage when the system is used in an irradiation room for particle therapy. There was no coincidence circuit and only singles list-mode data were acquired. The coincidence detection was done by software offline. Energy resolution was 14% and timing resolution was 4.4 ns. Therefore, we set the energy window to 400–600 keV and the coincidence timing window to 10 ns. For the random correction, we implemented the delayed coincidence method in the coincidence software. We also set a delayed coincidence timing window of 10 ns with the delay time of 128 ns.

TABLE I
BASIC SPECIFICATIONS OF THE SROP SYSTEM

Inner diameter	660 mm
Axial length	214 mm
Width of the open space	430 mm
Scintillator material	Zr-doped GSO (GSOZ)
Scintillator size	2.8×2.8×7.5 mm^3
Number of crystals per block	16×16×4
Block size of each detector	46×46×30 mm^3
Photo detector	64-ch super bialkali PMT
Number of detectors per ring	40
Number of rings	4

D. Basic Performance Evaluation

1) Absolute Sensitivity and Spatial Resolution: Absolute sensitivity and spatial resolution were measured with a ^{22}Na point source (0.16 MBq) for several positions with offsets toward the *x*, *y*, *z*, and *w* directions from the center of the gantry. We included the *w* direction for the evaluation in addition to the basic axes of *x*, *y*, and *z* because the *w* direction had the longest FOV width. The measurement was conducted once for each source location and each measurement time was 300 s. We used the filtered back projection (FBP) and the 3-D ordered subset expectation maximization (OSEM) [43]–[47] for image reconstruction. For both cases, we reconstructed images with and without DOI information to demonstrate the effect of the DOI detectors on spatial resolution. The voxel size was $1.5 \times 1.5 \times 1.5$ mm^3. For the FBP, using all LORs, we generated a 3-D sinogram with the radial sampling pitch of 1.5 mm, the number of radial samplings of 480, the number of angular samplings of 360, the axial slice thickness of 1.5 mm, and the number of axial slices of 150. An oblique sinogram was composed for each combination of the axial slice sampling positions assuming a 360 mm rotation radius. The maximum oblique angle was 17.3°. The direct slices of the 3-D sinogram were formed on the *w*-*y* plane, and the slice direction was set to the *v* direction (for axis directions, see Fig. 2) so as to be the same as the open mode of the small AS-type SROP prototype [6], which had transformable architecture to the SROP (open mode) and cylindrical PET

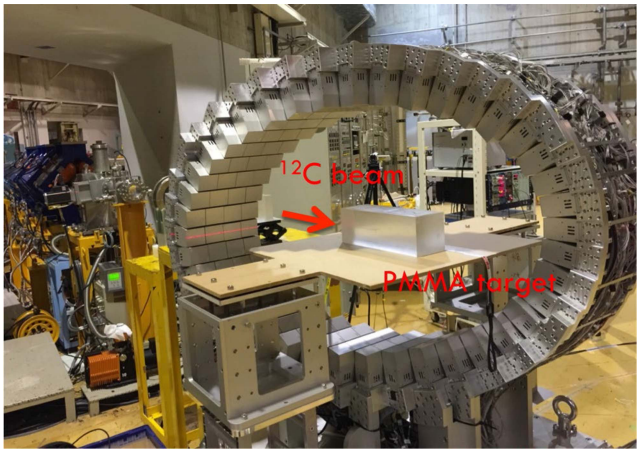

Fig. 4. In-beam experiment setup in HIMAC.

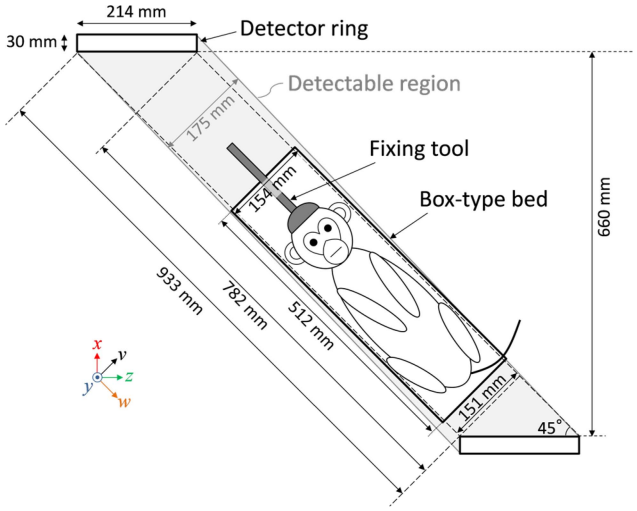

Fig. 5. Setup for the dynamic entire-body monkey imaging. The dimensions of the SROP system geometry in the central coronal slice are shown. The light gray color region indicates the region from which emitted annihilation photons can be detected.

(closed mode). Because the 3-D sinogram had data truncation depending on azimuthal and elevation angles, we filled the truncated region by reprojecting an FBP image reconstructed only from the direct sinograms. Then, the 3-D sinogram with the truncation regions filled in was converted to a stack of 2-D sinograms by the Fourier rebinning algorithm [48]. A ramp filter with no cut-off was applied for each 2-D sinogram. For the 3-D OSEM, a Gaussian function with the full width at half maximum (FWHM) of 2.5 mm was used for the detector response function model. The numbers of subsets and iterations were 8 and 10, respectively. According to the NEMA standard [49], spatial resolution was evaluated by measuring the FWHM. We should note that no LOR limitation was applied both for the FBP and the 3-D OSEM as well as the sensitivity measurement.

2) Count Rate Performance: Count rate performance was evaluated using a cylindrical phantom with an inner diameter of 800 mm, an outer diameter of 900 mm, an inner length of 160 mm, and an outer length of 180 mm. The phantom was filled with an ^{18}F solution and placed in the center region with its long axis along the w axis of the SROP system. Starting with the total radioactivity of 188 MBq, the 10-min measurement was repeated 30 times at 30-min intervals.

3) Small Rod Phantom Imaging: In order to assess resolution performance in iterative image reconstruction, we measured a small rod phantom, which had a similar structure to the micro-Derenzo phantom. The former phantom was composed of an outer hollow cylinder and an inner solid cylinder with a diameter of 36.1 mm and a length of 17.8 mm. The inner solid cylinder had cylindrical hole clusters for containing radioactivity solution with hole diameters of 1, 1.6, 2.2, 3.0, 4.0, and 4.8 mm, and the holes in each cluster were separated by a distance equal to the hole diameter. The phantom was filled with ^{18}F solution having a total radioactivity of 18.6 MBq. The phantom was placed at the center of the FOV and it was measured in three directions, in which rods were aligned along w, z, and y directions. For each direction, the measurement time was controlled so that the total numbers of decays were almost the same. Images were reconstructed by the 3-D OSEM with and without DOI information. The number of iterations was 10 with 8 subsets. Random correction was applied by the delayed coincidence method. Attenuation correction was applied by assuming an attenuation coefficient of 0.1 cm^{-1} for the shape of the phantom. Scatter correction was not applied.

E. In-Beam Experiment

We conducted an in-beam imaging experiment using a ^{12}C beam with several beam intensities in the HIMAC (Fig. 4). For each measurement, a cuboid polymethyl methacrylate (PMMA) phantom with the size of $100 \times 100 \times 300$ mm^3 was placed at the center of the SROP FOV, which was also at the isocenter of the HIMAC irradiation port. DAQ was started before the irradiation and continued for 20 min after the irradiation ended. The beam had a 3.3-s cycle of spill on (2.0 s) and off (1.3 s) times, in which the beam was actually irradiated only during the spill on time. In contrast to the spill on time in which a lot of prompt gamma rays were generated, resulting in random coincidence events, we could extract true coincidence events for the spill off time in addition to the measurement time immediately after the irradiation. We irradiated the phantom with the beam intensities of 10^6, 10^7, 10^8, and 10^9 pps (particles per second). The beam intensity of 10^9 is the highest beam intensity available for clinical treatment in the HIMAC. The beam energy was 400 MeV/u and 3 spills were irradiated for each measurement. The total numbers of irradiated particles for each measurement were calculated as $10^6 \times 3.3 \times 3$, $10^7 \times 3.3 \times 3$, $10^8 \times 3.3 \times 3$, and $10^9 \times 3.3 \times 3$. For the image reconstruction, the 3-D OSEM with eight subsets and ten iterations was applied with normalization, random, scatter, and attenuation corrections. Attenuation and scatter corrections were applied by assuming an attenuation map filled with the uniform linear attenuation coefficient of the PMMA for the shape of the phantom. For reconstructed images, peaks of radioactivity profiles in the beam direction were compared with a peak of the dose profile measured using an ionization chamber in a water tank and converted to the PMMA equivalent.

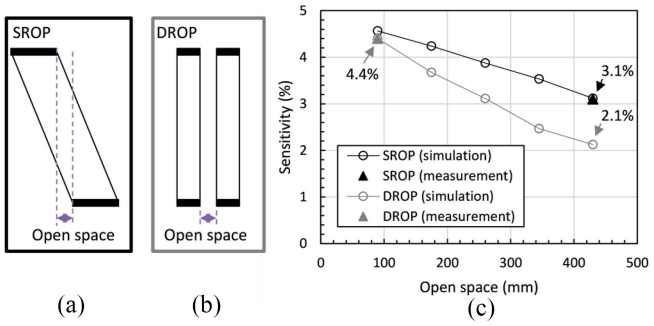

Fig. 6. Schematic illustrations showing the open space for SROP (a) and DROP (b). A comparison plot of the sensitivity at the FOV center for SROP and DROP while varying the open space (c). The sensitivity at the FOV center was estimated by a Monte Carlo simulation normalized with the measured sensitivity of the DROP system. Measured sensitivities of the SROP system with the 430-mm open space and the DROP system with the 90-mm open space [7] are also shown.

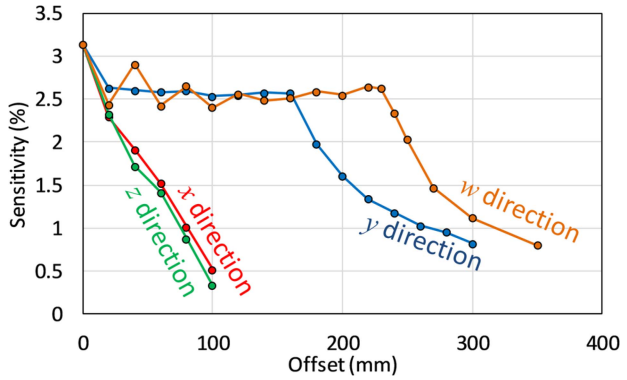

Fig. 7. Absolute sensitivity measured with offsets along x, y, z, and w directions.

F. Dynamic Entire-Body Monkey Imaging

For the animal experiment, the system was moved to an animal experiment room where such experiments with radioactivity injection were allowed in a radiation-controlled area. We demonstrated simultaneous total-body monkey imaging by making full use of the wide oval FOV of the SROP system having a longitudinal length of the elliptical opening longer than 900 mm. Fig. 5 shows an experimental setup with the SROP system geometry. For the illustrated setup, we could achieve an oval cylindrical FOV with lengths of 782 mm in the major axis direction and 660 mm in the minor axis direction. We note that the region in which annihilation gamma rays are detectable is slightly wider than the area calculated only using the detector length of 214 mm because of the thickness of the block detector. We measured a male monkey (*Macaca fascicularis*, 2.76 kg) while it was lying on a portable box-type bed under an anesthetized condition, and the top of the monkey head was fixed with restraints onto the bed. The monkey was positioned along the w direction with its head centered at the FOV. The monkey was injected with 50 MBq FDG at the start of the 35-min measurement. The obtained list-mode data were divided into time frames. The 3-D OSEM with eight subsets and ten iterations was applied for each frame with normalization, random, scatter and attenuation corrections. The attenuation map used for the scatter and attenuation corrections was generated by segmenting a PET image reconstructed without these corrections into monkey-body regions and other regions. The monkey-body regions were filled with the water equivalent attenuation coefficient. This experiment was approved by the local ethical committee of NIRS-QST and carried out in compliance with the institute's animal experimentation guidelines.

III. Results

A. Sensitivity Prediction

Fig. 6 shows the simulation results normalized with the actual measured sensitivity of the DROP system with the open space of 90 mm. The predicted sensitivity was 3.1% with 430 mm open space for SROP, which was 1.5 times higher than for DROP with the same open space. We also plot sensitivity measured at the center of the FOV of the developed SROP system in the same figure. The predicted sensitivity agreed well with the measured sensitivity. The results showed that SROP achieved higher sensitivity than DROP for various possible open spaces with the same number of detectors, and the sensitivity difference became large when the open space was large. We should note that the DROP with the open space larger than 100 mm had a discontinuous axial FOV as it exceeded the axial width of one side of the dual-ring configuration.

B. Basic Performance Evaluation

1) Absolute Sensitivity and Spatial Resolution: Fig. 7 shows the sensitivity profiles for the ^{22}Na point source. The peak sensitivity obtained at the central position of the FOV was 3.1%, which agreed well with the already mentioned sensitivity simulation shown in Fig. 6. Offsets with sensitivity better than 2% were 180 mm for the y direction and 250 mm for the w direction, which corresponded to ranges of 360 mm and 500 mm, respectively. Even with 350 mm offset, the sensitivity was 0.8% in the w direction, which indicated a 700-mm long wide FOV. We observed a fluctuation in the w direction which we attributed to be due to the detector arrangement pattern making a peak at the middle point between a detector pair and valleys for gaps in neighboring detectors.

Fig. 8 shows point source images reconstructed by the FBP and the 3-D OSEM with and without DOI information after summing all data measured by placing the point source at several positions. With the DOI information, all the points were clearly reconstructed while points located off center positions in y and w directions were blurred. Fig. 9 shows spatial resolutions as the mean value of the FWHMs in radial, tangential and axial directions for the reconstructed images. Average FWHM values with standard deviations for the 3-D OSEM, 3-D OSEM without DOI information, FBP, and FBP without DOI information were 2.6±0.2, 3.8±0.5, 6.5±0.8, and 8.7±2.0 mm, respectively, for all the measured locations; and, when we considered only offsets less than or equal to 100 mm, those values were 2.6±0.3, 3.4±0.3, 6.0±0.2, and

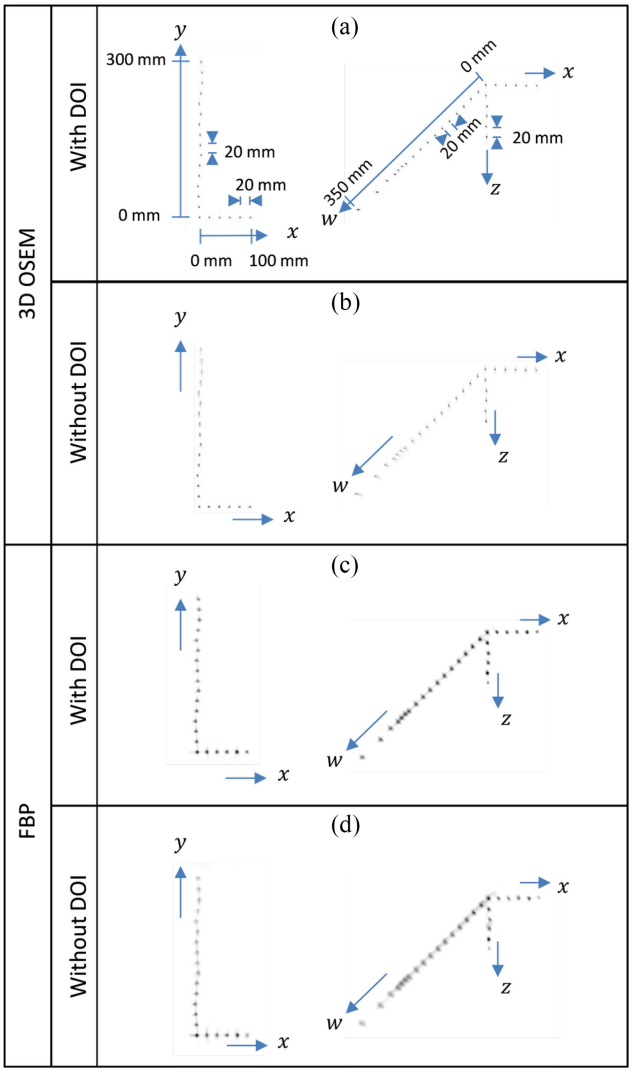

Fig. 8. Reconstructed images for point source measurements summed into one histogram for image reconstruction. Images were reconstructed by 3-D OSEM with (a) and without DOI information (b) and by FBP with (c) and without DOI information (d).

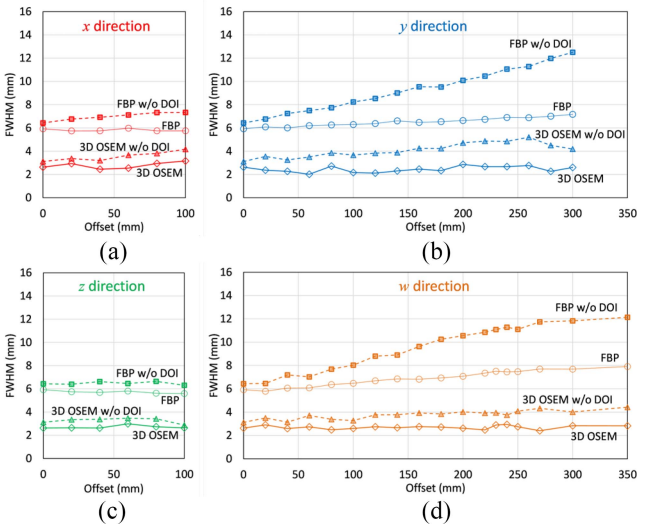

Fig. 9. Spatial resolution (FWHM) measured at several offsets along x (a), y (b), z (c), and w (d) directions for images reconstructed by FBP without DOI information (FBP w/o DOI), FBP with DOI information (FBP), 3-D OSEM without DOI information (3-D OSEM w/o DOI), and 3-D OSEM with DOI information (3-D OSEM).

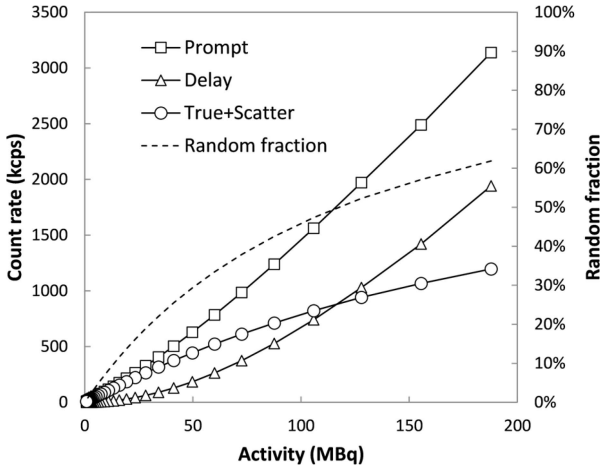

Fig. 10. Count rate performance of the SROP system.

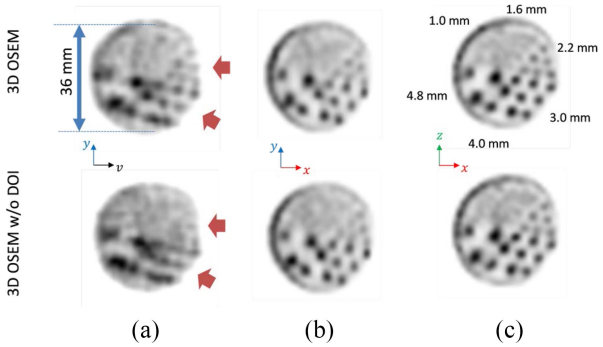

Fig. 11. Reconstructed images for the small rod phantom placed along the w (a), z (b), and y (c) directions. Upper and lower rows show images reconstructed with (3-D OSEM) and without (3-D OSEM w/o DOI) DOI information, respectively.

7.0±0.5 mm, respectively. The spatial resolution results indicated that, without the DOI information, the larger the offset was, the lower the spatial resolution except for the z direction. With the DOI information, the degradation of the spatial resolution was mitigated for the FBP results, and the spatial resolution was almost uniform for the 3-D OSEM results.

2) Count Rate Performance: Fig. 10 shows count rate performance of the SROP system. Event rate for the true and scatter events (true + scatter) was estimated by subtracting the delayed event count from the prompt event count. The random fraction was estimated by dividing the delayed event count by the prompt event count. Calculating by interpolation, we found the true + scatter event rates were equal to the random rates at 116 MBq with the count rate of 880 kcps.

3) Small Rod Phantom Imaging: Fig. 11 shows images of the small rod phantom reconstructed with and without DOI information by using the 3-D OSEM with eight subsets and ten iterations. The central single slice perpendicular to the rod direction is shown for each reconstructed image. There was a circular frame in each reconstructed image surrounding the rods, which was caused by the structure of the phantom having a small gap between the outer hollow cylinder and the

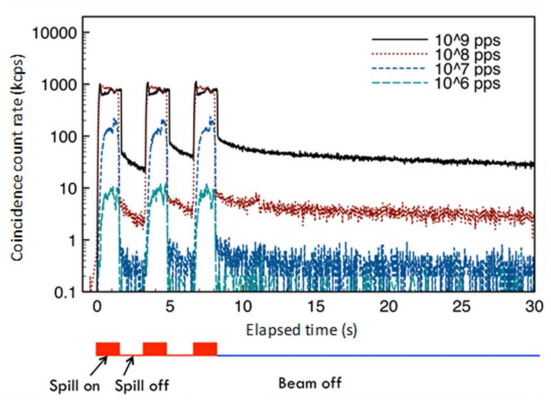

Fig. 12. Coincidence count rates for the in-beam experiments with PMMA phantom irradiated by ^{12}C beams with several intensities in HIMAC and measured during and after the irradiation. Only the first 30 s period was plotted to show the count rate response for the spill on time.

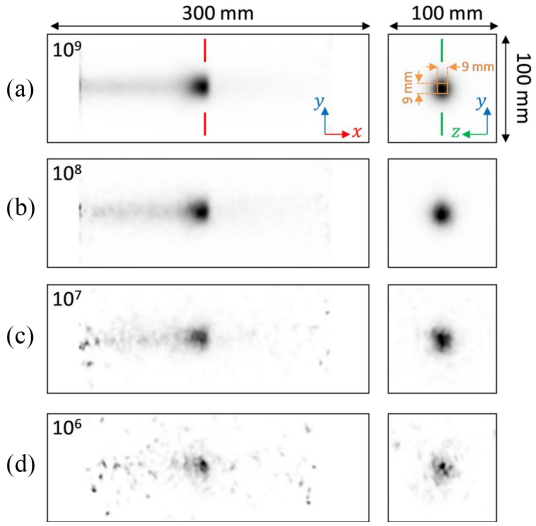

Fig. 13. Images reconstructed for the HIMAC in-beam PET experiment using ^{12}C beams with several beam intensities of 10^9 (a), 10^8 (b), 10^7 (c), and 10^6 (d) pps shown as the x-y slice at $z = 0$ mm (left) and the y-z slice at $x = -3$ mm (right). For each image, boxes colored in black indicate the size of the PMMA phantom. The orange box in (a) indicates the ROI for profile analysis.

inner solid cylinder. Because of the bias of original liquid inclusion into the small gaps, there was a truncation in the circular frame in each image. The images in Fig. 11(a), in which the rods were aligned along the w direction, were generated by subsampling to half voxel size and rotating around the y-axis by 45° with bilinear interpolation. Total radioactivity in the phantom at the starting time and measurement time for measurements with rods along the w, z, and y directions were 18.6 MBq and 14 min, 16.0 MBq and 16 min, and 13.3 MBq and 20 min, respectively; and the number of measured counts (true + scatter) and the random fractions were 270 M counts and 6.4%, 275 M counts and 5.4%, and 273 M counts and 4.6%, respectively. We note that the true + scatter counts were calculated by subtracting delayed coincidence counts from prompt coincidence counts. The results showed that the 2.2-mm rods were resolved when the rods were along the z and y directions [Fig. 11(b) and (c)] even without DOI information. When the rods were along the w direction [Fig. 11(a)], without DOI information, 2.2-mm rods were not resolved, and separation of 3.0-mm rods was not clear. On the other hand, both 2.2-mm and 3.0-mm rods were resolved with DOI information [arrows in Fig. 11(a)].

C. In-Beam Experiment

Fig. 12 shows coincidence count rates obtained in the in-beam experiment with ^{12}C beams irradiated in the HIMAC. When the beam intensity was 10^8 and 10^9 pps, the coincidence count rate was saturated during the spill on time, while it was not saturated for 10^6 and 10^7 pps even during the spill on time. Except for the spill on time, the coincidence count rates were proportional to the beam intensity. For each irradiation, we extracted coincidence list-mode data for the spill off time and immediately after the irradiation (beam off time). The numbers of list-mode counts (true + scatter) and random fractions, respectively, were 11 k counts and 0.07% for 10^6 pps, 74 k counts and 0.1% for 10^7 pps, 829 k counts and 0.8% for 10^8 pps, and 7.6 M counts and 4.9% for 10^9 pps. Fig. 13 shows the images reconstructed from the list-mode data shown with the shape of the PMMA phantom.

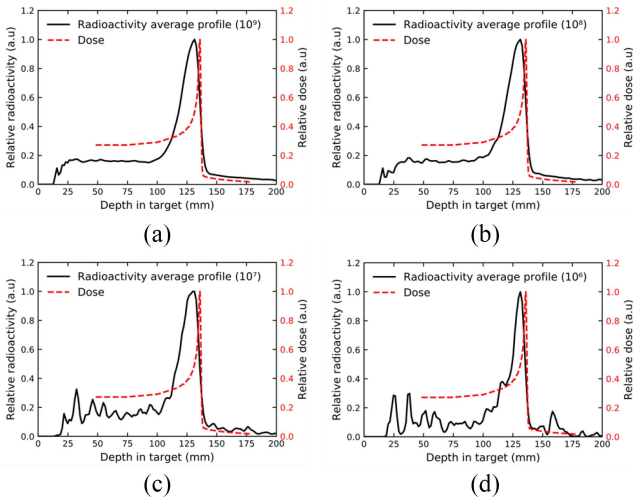

Fig. 14. Profiles for the doses and reconstructed PET images along the beam direction with the beam intensities of 10^9(a), 10^8(b), 10^7(c), and 10^6(d) pps. Difference of the peaks between the radioactivity average profile and the dose was 4.6 mm for all case.

We analyzed radioactivity profiles along the beam direction (x direction) for the region of interest (ROI) indicated in Fig. 13 for each image. Fig. 14 shows profiles of the radioactivity on images for several beam intensities along the beam direction plotted with the dose profile measured using the ionization chamber. Differences in peaks of the dose and PET images were 4.6 mm for all cases.

D. Dynamic Entire-Body Monkey Imaging

For the 35-min measurement, a total of 706 M true + scatter counts with the random fraction of 32% was obtained. Fig. 15 shows the dynamic image of the monkey obtained with FDG as the maximum intensity projection (MIP) images [Fig. 15(a)] and the representative coronal slices, including

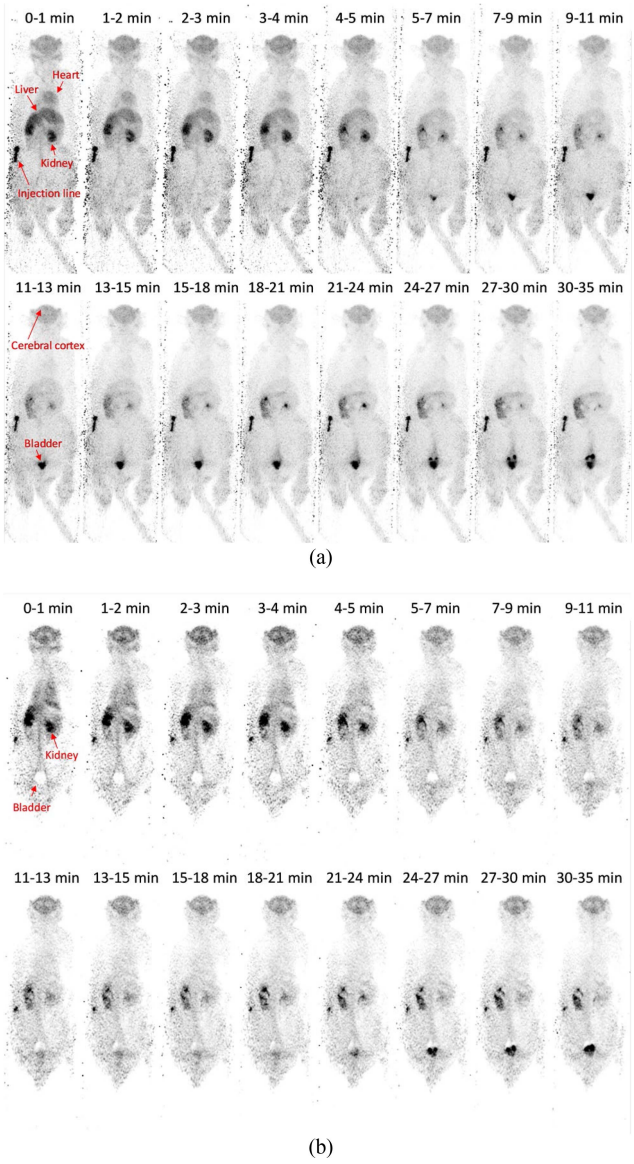

Fig. 15. MIP images (a) and coronal single slice images at $y = -15$ mm (b) for each time frame of the dynamic entire-body monkey imaging.

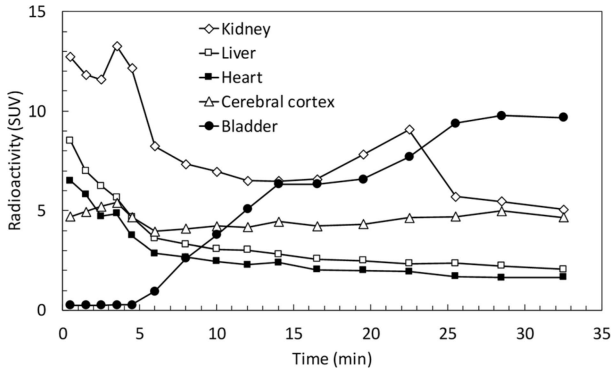

Fig. 16. TACs for monkey organs during the dynamic imaging.

the kidney and bladder [Fig. 15(b)]. Fig. 16 shows the time activity curve (TAC) for organs. The heart, liver and kidney of the monkey were clearly imaged at various time frames after a bolus injection of FDG. Dynamic changes in the tracer distribution were observed. For example, we observed from images and the TAC that the concentration in the kidney at the end of the first 5 min was moved to the bladder.

IV. Discussion

The developed human-sized SROP system had the open space of 430 mm, which was 4.8 times wider than that of the human-sized DROP system [7] having a 90 mm open space at the cost of a 30% sensitivity loss [3.1% absolute sensitivity at the FOV center (Fig. 7) for the SROP of the 430 mm open space and 4.4% for the DROP of the 90 mm open space]. We should note that, although the sensitivity was dropped, the effectiveness of the SROP geometry in achieving 1.5 times higher sensitivity compared with the DROP geometry composed of the same number of detectors with the same ring diameter and the same width of the open space was confirmed by simulation [Fig. 6(c)]. We also note that the measured sensitivity at the FOV center agreed well with the simulation.

To demonstrate the effectiveness of the DOI detectors for SROP, we evaluated the spatial resolution with the FBP and 3-D OSEM each with and without DOI information. The spatial resolution of less than 3 mm for the entire FOV was achieved by the 3-D OSEM while it was significantly degraded without DOI information. The results showed that the DOI information was effective for improving spatial resolution even at the central region within 100-mm offset. This was also demonstrated by the small rod phantom imaging experiment. When the rods of the phantom were along the w direction, the 3-mm rods were not clearly resolved without DOI information. On the other hand, the 3-mm rods were clearly resolved, and even the 2.2-mm rods were resolved with DOI information. This was because most of the crystals were oblique for the v direction and the DOI information was essential for achieving high spatial resolution along that direction.

We should note that, in this article, we only measured sensitivity, spatial resolution, and count rate performance for a quantitative evaluation. The NEMA-based image quality, count rate, and scatter fraction performance were not measured. Although we believe the current measurement set was enough for a proof-of-concept of the human-scale SROP system, the limitation of this article is the lack of thorough performance measurements. In our future work, we will assess the applicability of the NEMA protocols to the SROP system, carry out further performance evaluation in accordance with the protocols for systematic assessment, and make performance comparisons against other systems. For the comparison, the tilted configuration of the SROP system should be considered, and it would be important to compare performance measurements regarding the v direction, which were omitted in this article, with the axial direction of cylindrical PET systems. The spatial resolution and sensitivity along the v direction and imaging performance for the rod phantom where the rods are aligned along the v-direction will be measured.

The system had wheels for easy transport to experiment rooms with different apparatuses and regulations. Therefore, we could carry out measurements in the HIMAC and the

animal experiment room. A human-scale PET system with such mobility and versatility is unique.

In the HIMAC experiment, we used ^{12}C beams up to the maximum intensity actually used in cancer treatment. In our previous experiments using the DROP system [7], we tested beams only up to 10^8 pps because the open space was only 90 mm long and too strong a beam could cause severe damage to detectors close downstream in the beam line where a lot of secondary particles were scattered. The wide-open space of the SROP system allowed us to use the maximum beam intensity of 10^9 pps, and we have observed no damage so far. As a result of the offline software coincidence detection, we could extract list-mode data for spill off time and the time immediately after the irradiation, although the coincidence count rate was saturated during the spill on time. The reconstructed images showed clear peaks shifted 4.6 mm toward the proximal position from the dose peak position. These differences between peaks of the dose of ^{12}C irradiation and the radioactivity produced via nuclear fragmentation reactions agreed with previous measurements and modeling results [9], [15]. Therefore, our system had the capability for in-beam measurement for dose verification at practical particle therapy conditions.

The FDG monkey dynamic imaging experiment was conducted in the animal experiment room of a radiation-controlled area. The FOV size was large enough to measure the entire body of the monkey for the dynamic scan as the sensitivity profile along the *w* direction in Fig. 7 showed that the system had a 700-mm long region with sensitivity of better than 0.8%. We should note that Fig. 9 showed the region had almost uniform spatial resolution with DOI information. The radioactivity distribution changes for individual organs were observed with sufficient image quality for each time frame.

Because of the wide-open space and mobility, the system can be used to study the washout effect using animals [50]–[54]. It has been suggested that radioactive ion beams are useful for washout studies [55]–[58]. Therefore, our future work with the developed system will include a washout study with radioactive ion beams and entire-body scanning of animals.

Finally, the system has the gantry size large enough for human subjects and the open space wide enough for a heavy-ion beam to pass through with a sufficient margin to avoid radiation damage to detectors. As we showed by Monte Carlo simulation [59], the online measurement for dose verification by the SROP system had advantages over offline measurement. Therefore, we will also make in-beam PET measurements in a progression toward more precise patient treatment in HIMAC.

V. Conclusion

We developed the multiuse human-scale SROP system having the large open space of 430 mm and the wide FOV longer than 700 mm with sufficiently good sensitivity. The system can be easily moved to different experiment rooms and that also allows for multipurpose uses. The system has versatile capabilities for PET applications requiring high sensitivity and high spatial resolution throughout the FOV.

References

[1] T. Yamaya *et al.*, "A proposal of an open PET geometry," *Phys. Med. Biol.*, vol. 53, no. 3, pp. 757–773, Feb. 2008, doi: 10.1088/0031-9155/53/3/015.

[2] T. Yamaya *et al.*, "Development of a small prototype for a proof-of-concept of OpenPET imaging," *Phys. Med. Biol.*, vol. 56, no. 4, pp. 1123–1137, 2011, doi: 10.1088/0031-9155/56/4/015.

[3] H. Tashima, T. Yamaya, E. Yoshida, S. Kinouchi, M. Watanabe, and E. Tanaka, "A single-ring OpenPET enabling PET imaging during radiotherapy," *Phys. Med. Biol.*, vol. 57, no. 14, pp. 4705–4718, Jul. 2012, doi: 10.1088/0031-9155/57/14/4705.

[4] S. Kinouchi *et al.*, "Simulation design of a single-ring OpenPET for in-beam PET," in *Proc. IEEE NSS MIC Conf. Rec.*, Valencia, Spain, 2011, pp. 3481–3483, doi: 10.1109/NSSMIC.2011.6152638.

[5] E. Yoshida *et al.*, "Development of a single-ring OpenPET prototype," *Nucl. Instrum. Methods Phys. Res. Sect. A, Accelerators Spectrometers Detectors Assoc. Equip.*, vol. 729, pp. 800–808, Nov. 2013, doi: 10.1016/j.nima.2013.08.041.

[6] H. Tashima *et al.*, "Development of a small single-ring OpenPET prototype with a novel transformable architecture," *Phys. Med. Biol.*, vol. 61, no. 4, pp. 1795–1809, 2016, doi: 10.1088/0031-9155/61/4/1795.

[7] E. Yoshida *et al.*, "Development of a whole-body dual ring OpenPET for in-beam PET," *IEEE Trans. Radiat. Plasma Med. Sci.*, vol. 1, no. 4, pp. 293–300, Jul. 2017, doi: 10.1109/TRPMS.2017.2703823.

[8] T. Yamaya and H. Tashima, "OpenPET enabling PET imaging during radiotherapy," in *Personalized Pathway-Activated Systems Imaging in Oncology*, T. Inoue, D. Yang, and G. Huang, Eds. Singapore: Springer, 2017, pp. 55–84.

[9] J. Pawelke *et al.*, "In-beam PET imaging for the control of heavy-ion tumour therapy," *IEEE Trans. Nucl. Sci.*, vol. 44, no. 4, pp. 1492–1498, Aug. 1997, doi: 10.1109/23.632694.

[10] K. Parodi, W. Enghardt, and T. Haberer, "In-beam PET measurements of beta+ radioactivity induced by proton beams," *Phys. Med. Biol.*, vol. 47, pp. 21–36, Jan. 2002, doi: 10.1088/0031-9155/47/1/302.

[11] K. Parodi, T. Bortfeld, and T. Haberer, "Comparison between in-beam and offline positron emission tomography imaging of proton and carbon ion therapeutic irradiation at synchrotron- and cyclotron-based facilities," *Int. J. Radiat. Oncol. Biol. Phys.*, vol. 71, no. 3, pp. 945–956, Jul. 2008, doi: 10.1016/j.ijrobp.2008.02.033.

[12] P. Crespo, G. Shakirin, and W. Enghardt, "On the detector arrangement for in-beam PET for hadron therapy monitoring," *Phys. Med. Biol.*, vol. 51, no. 9, pp. 2143–2163, May 2006, doi: 10.1088/0031-9155/51/9/002.

[13] Y. Iseki *et al.*, "Positron camera for range verification of heavy-ion radiotherapy," *Nucl. Instrum. Methods Phys. Res. A, Accelerators Spectrometers Detectors Assoc. Equip.*, vol. 515, no. 3, pp. 840–849, Dec. 2003, doi: 10.1016/j.nima.2003.07.005.

[14] W. Enghardt *et al.*, "Charged hadron tumour therapy monitoring by means of PET," *Nucl. Instrum. Methods Phys. Res. A, Accelerators Spectrometers Detectors Assoc. Equip.*, vol. 525, nos. 1–2, pp. 284–288, Jun. 2004, doi: 10.1016/j.nima.2004.03.128.

[15] F. Pönisch, K. Parodi, B. G. Hasch, and W. Enghardt, "The modelling of positron emitter production and PET imaging during carbon ion therapy," *Phys. Med. Biol.*, vol. 49, no. 23, pp. 5217–5232, Dec. 2004, doi: 10.1088/0031-9155/49/23/002.

[16] T. Inaniwa *et al.*, "Experimental determination of particle range and dose distribution in thick targets through fragmentation reactions of stable heavy ions," *Phys. Med. Biol.*, vol. 51, no. 17, pp. 4129–4146, Sep. 2006, doi: 10.1088/0031-9155/51/17/002.

[17] T. Nishio, T. Ogino, K. Nomura, and H. Uchida, "Dose-volume delivery guided proton therapy using beam on-line PET system," *Med. Phys.*, vol. 33, no. 11, pp. 4190–4197, 2006, doi: 10.1118/1.2361079.

[18] T. Nishio, A. Miyatake, T. Ogino, K. Nakagawa, N. Saijo, and H. Esumi, "The development and clinical use of a beam on-line PET system mounted on a rotating gantry port in proton therapy," *Int. J. Radiat. Oncol. Biol. Phys.*, vol. 76, no. 1, pp. 277–286, Jan. 2010, doi: 10.1016/j.ijrobp.2009.05.065.

[19] F. Fiedler *et al.*, "On the effectiveness of ion range determination from in-beam PET data," *Phys. Med. Biol.*, vol. 55, no. 7, pp. 1989–1998, Apr. 2010, doi: 10.1088/0031-9155/55/7/013.

[20] S. Surti, W. Zou, M. E. Daube-Witherspoon, J. McDonough, and J. S. Karp, "Design study of an *in situ* PET scanner for use in proton beam therapy," *Phys. Med. Biol.*, vol. 56, no. 9, pp. 2667–2685, May 2011, doi: 10.1088/0031-9155/56/9/002.

[21] T. Hofmann *et al.*, "Dose reconstruction from PET images in carbon ion therapy: A deconvolution approach," *Phys. Med. Biol.*, vol. 64, no. 2, Jan. 2019, Art. no. 025011, doi: 10.1088/1361-6560/aaf676.

[22] V. Ferrero *et al.*, "Evaluation of in-beam PET treatment verification in proton therapy with different reconstruction methods," *IEEE Trans. Radiat. Plasma Med. Sci.*, vol. 4, no. 2, pp. 202–211, Mar. 2020, doi: 10.1109/trpms.2019.2942713.

[23] Y. Zhong *et al.*, "Novel online PET imaging for intrabeam range verification and delivery optimization: A simulation feasibility study," *IEEE Trans. Radiat. Plasma Med. Sci.*, vol. 4, no. 2, pp. 212–217, Mar. 2020, doi: 10.1109/trpms.2019.2950231.

[24] A. Topi *et al.*, "Monitoring proton therapy through in-beam PET: An experimental phantom study," *IEEE Trans. Radiat. Plasma Med. Sci.*, vol. 4, no. 2, pp. 194–201, Mar. 2020, doi: 10.1109/trpms.2019.2924036.

[25] F. Roellinghoff *et al.*, "Real-time proton beam range monitoring by means of prompt-gamma detection with a collimated camera," *Phys. Med. Biol.*, vol. 59, no. 5, pp. 1327–1338, Feb. 2014, doi: 10.1088/0031-9155/59/5/1327.

[26] P. C. Lopes *et al.*, "Time-resolved imaging of prompt-gamma rays for proton range verification using a knife-edge slit camera based on digital photon counters," *Phys. Med. Biol*, vol. 60, pp. 6063–6085, Jul. 2015, doi: 10.1088/0031-9155/60/15/6063.

[27] C. Richter *et al.*, "First clinical application of a prompt gamma based in vivo proton range verification system," *Radiother. Oncol.*, vol. 118, no. 2, pp. 232–237, Feb. 2016, doi: 10.1016/j.radonc.2016.01.004.

[28] H. Zhang *et al.*, "Design and performance evaluation of a BGO + SiPM detector for high-energy prompt gamma imaging in proton therapy monitoring," *IEEE Trans. Radiat. Plasma Med. Sci.*, vol. 4, no. 2, pp. 184–193, Mar. 2020, doi: 10.1109/trpms.2020.2972594.

[29] C. Golnik *et al.*, "Range assessment in particle therapy based on prompt γ-ray timing measurements," *Phys. Med. Biol.*, vol. 59, no. 18, pp. 5399–5422, Sep. 2014, doi: 10.1088/0031-9155/59/18/5399.

[30] T. Werner *et al.*, "Processing of prompt gamma-ray timing data for proton range measurements at a clinical beam delivery," *Phys. Med. Biol.*, vol. 64, no. 10, May 2019, Art. no. 105023, doi: 10.1088/1361-6560/ab176d.

[31] H. Seo *et al.*, "Experimental performance of double-scattering Compton camera with anthropomorphic phantom," *J. Instrum.*, vol. 6, no. 1, Jan. 2011, Art. no. C01024, doi: 10.1088/1748-0221/6/01/C01024.

[32] S. Kurosawa *et al.*, "Prompt gamma detection for range verification in proton therapy," *Current Appl. Phys.*, vol. 12, no. 2, pp. 364–368, Mar. 2012, doi: 10.1016/j.cap.2011.07.027.

[33] J. Krimmer *et al.*, "Development of a Compton camera for medical applications based on silicon strip and scintillation detectors," *Nucl. Instrum. Methods Phys. Res. A, Accelerators Spectrometers Detectors Assoc. Equip.*, vol. 787, pp. 98–101, Jul. 2015, doi: 10.1016/j.nima.2014.11.042.

[34] M. Fontana *et al.*, "Monitoring ion beam therapy with a Compton camera: Simulation studies of the clinical feasibility," *IEEE Trans. Radiat. Plasma Med. Sci.*, vol. 4, no. 2, pp. 218–232, Mar. 2020, doi: 10.1109/trpms.2019.2933985.

[35] N. Kohlhase *et al.*, "Capability of MLEM and OE to detect range shifts with a Compton camera in particle therapy," *IEEE Trans. Radiat. Plasma Med. Sci.*, vol. 4, no. 2, pp. 233–242, Mar. 2020, doi: 10.1109/trpms.2019.2937675.

[36] H. Murayama, H. Ishibashi, H. Uchida, T. Omura, and T. Yamashita, "Depth encoding multicrystal detectors for PET," *IEEE Trans. Nucl. Sci.*, vol. 45, no. 3, pp. 1152–1157, Jun. 1998, doi: 10.1109/23.681994.

[37] T. Tsuda *et al.*, "A four-layer depth of interaction detector block for small animal PET," *IEEE Trans. Nucl. Sci.*, vol. 51, no. 5, pp. 2537–2542, Oct. 2004, doi: 10.1109/TNS.2004.835739.

[38] T. Yamaya *et al.*, "Preliminary resolution performance of the prototype system for a 4-Layer DOI-PET scanner: jPET-D4," *IEEE Trans. Nucl. Sci.*, vol. 53, no. 3, pp. 1123–1128, Jun. 2006, doi: 10.1109/TNS.2006.871901.

[39] Y. Hirano *et al.*, "Performance evaluation of a depth-of-interaction detector by use of position-sensitive PMT with a super-bialkali photocathode," *Radiol. Phys. Technol.*, vol. 7, no. 1, pp. 57–66, Jan. 2014, doi: 10.1007/s12194-013-0231-4.

[40] Y. Yoshii *et al.*, "Integrated treatment using intraperitoneal radioimmunotherapy and positron emission tomography-guided surgery with ^{64}Cu-labeled cetuximab to treat early- and late-phase peritoneal dissemination in human gastrointestinal cancer xenografts," *Oncotarget*, vol. 9, no. 48, pp. 28935–28950, 2018, doi: 10.18632/oncotarget.25649.

[41] G. Akamatsu *et al.*, "Performance evaluation of a whole-body prototype PET scanner with four-layer DOI detectors," *Phys. Med. Biol.*, vol. 64, no. 9, Apr. 2019, Art. no. 095014, doi: 10.1088/1361-6560/ab18b2.

[42] S. Agostinelli *et al.*, "Geant4—A simulation toolkit," *Nucl. Instrum. Methods Phys. Res. A, Accelerators Spectrometers Detectors Assoc. Equip.*, vol. 506, no. 3, pp. 250–303, Jul. 2003, doi: 10.1016/S0168-9002(03)01368-8.

[43] L. A. Shepp and Y. Vardi, "Maximum likelihood reconstruction for emission tomography," *IEEE Trans. Med. Imag.*, vol. 1, no. 2, pp. 113–122, Oct. 1982, doi: 10.1109/TMI.1982.4307558.

[44] H. M. Hudson and R. S. Larkin, "Accelerated image reconstruction using ordered subsets of projection data," *IEEE Trans. Med. Imag.*, vol. 13, no. 4, pp. 601–609, Dec. 1994, doi: 10.1109/42.363108.

[45] A. J. Reader, K. Erlandsson, M. A. Flower, and R. J. Ott, "Fast accurate iterative reconstruction for low-statistics positron volume imaging," *Phys. Med. Biol.*, vol. 43, pp. 835–846, Apr. 1998, doi: 10.1088/0031-9155/43/4/012.

[46] L. C. Parra and H. H. Barrett, "List-mode likelihood: EM algorithm and image quality estimation demonstrated on 2-D PET," *IEEE Trans. Med. Imag.*, vol. 17, no. 2, pp. 228–235, Apr. 1998, doi: 10.1109/42.700734.

[47] A. Rahmim, J. C. Cheng, S. Blinder, M. L. Camborde, and V. Sossi, "Statistical dynamic image reconstruction in state-of-the-art high-resolution PET," *Phys. Med. Biol.*, vol. 50, no. 20, pp. 4887–4912, 2005, doi: 10.1088/0031-9155/50/20/010.

[48] M. Defrise, P. Kinahan, D. W. Townsend, C. Michel, M. Sibomana, and D. Newport, "Exact and approximate rebinning algorithms for 3-D PET data," *IEEE Trans. Med. Imag.*, vol. 16, no. 2, pp. 145–158, Apr. 1997, doi: 10.1109/42.563660.

[49] *Performance Measurements of Positron Emission Tomography (PET)*, Standard NEMA NU 2-2018, 2018.

[50] Y. Hirano *et al.*, "Compartmental analysis of washout effect in rat brain: In-beam OpenPET measurement using a ^{11}C beam," *Phys. Med. Biol.*, vol. 58, no. 23, pp. 8281–8294, Dec. 2013, doi: 10.1088/0031-9155/58/23/8281.

[51] C. Toramatsu *et al.*, "Washout effect in rabbit brain: In-beam PET measurements using^{10}C, ^{11}C and^{15}O ion beams," *Biomed. Phys. Eng. Exp.*, vol. 4, no. 3, 2018, Art. no. 035001, doi: 10.1088/2057-1976/aaade7.

[52] C. Ammar *et al.*, "Comparing the biological washout of β+-activity induced in mice brain after 12C-ion and proton irradiation," *Phys. Med. Biol.*, vol. 59, no. 23, pp. 7229–7244, 2014, doi: 10.1088/0031-9155/59/23/7229.

[53] T. Tomitani *et al.*, "Washout studies of 11C in rabbit thigh muscle implanted by secondary beams of HIMAC," *Phys. Med. Biol.*, vol. 48, no. 7, pp. 875–889, Apr. 2003, doi: 10.1088/0031-9155/48/7/305.

[54] H. Mizuno *et al.*, "Washout measurement of radioisotope implanted by radioactive beams in the rabbit," *Phys. Med. Biol.*, vol. 48, no. 15, pp. 2269–2281, Aug. 2003, doi: 10.1088/0031-9155/48/15/302.

[55] M. Kanazawa *et al.*, "Application of an RI-beam for cancer therapy: In-vivo verification of the ion-beam range by means of positron imaging," *Nucl. Phys. A*, vol. 701, nos. 1–4, pp. 244–252, Apr. 2002, doi: 10.1016/S0375-9474(01)01592-5.

[56] Y. Iseki *et al.*, "Range verification system using positron emitting beams for heavy-ion radiotherapy," *Phys. Med. Biol.*, vol. 49, no. 14, pp. 3179–3195, Jul. 2004, doi: 10.1088/0031-9155/49/14/012.

[57] A. Mohammadi *et al.*, "Production of an ^{15}O beam using a stable oxygen ion beam for in-beam PET imaging," *Nucl. Instrum. Methods Phys. Res. A, Accelerators Spectrometers Detectors Assoc. Equip.*, vol. 849, pp. 76–82, Mar. 2017, doi: 10.1016/j.nima.2016.12.028.

[58] A. Mohammadi *et al.*, "Range verification of radioactive ion beams of ^{11}C and ^{15}O using in-beam PET imaging," *Phys. Med. Biol.*, vol. 64, no. 14, 2019, Art. no. 145014, doi: 10.1088/1361-6560/ab25ce.

[59] H. Tashima, C. Kurz, E. Yoshida, J. Debus, K. Parodi, and T. Yamaya, "Patient data-based Monte–Carlo simulation of in-beam single-ring OpenPET imaging," in *Proc. IEEE Nucl. Sci. Symp. Med. Imag. Conf. (NSS/MIC)*, San Diego, CA, USA, 2016, pp. 1–3, doi: 10.1109/NSSMIC.2015.7582137.